Title

Rapid aqueous-phase dark reaction of phenols with nitrosonium ions: Novel mechanism for atmospheric nitrosation and nitration at low pH.

Journal

PNAS Nexus, 3(9)

Authors

Cai, Baohua

Wang, Yixiang

Yang, Xin

et al.

Publication Date

2024-09-01

DOI

10.1093/pnasnexus/pgae385

Peer reviewed

PNAS Nexus, 2024, 3, pgae385
https://doi.org/10.1093/pnasnexus/pgae385
Advance access publication 6 September 2024
Research Report

Rapid aqueous-phase dark reaction of phenols with nitrosonium ions: Novel mechanism for atmospheric nitrosation and nitration at low pH

Baohua Cai[a], Yixiang Wang[a], Xin Yang[a,b,*], Yanchen Li[a], Jinghao Zhai[a,b], Yaling Zeng[a,b], Jianhuai Ye[a,b], Lei Zhu[a,b], Tzung-May Fu[a,b] and Qi Zhang[c,*]

[a]Shenzhen Key Laboratory of Precision Measurement and Early Warning Technology for Urban Environmental Health Risks, School of Environmental Science and Engineering, Southern University of Science and Technology, Shenzhen, Guangdong 518055, China
[b]Provincial Observation and Research Station for Coastal Atmosphere and Climate of the Greater Bay Area, Shenzhen 518055, China
[c]Department of Environmental Toxicology, University of California, Davis, CA 95616, USA
*To whom correspondence should be addressed: Email: yangx@sustech.edu.cn (X.Y.); dkwzhang@ucdavis.edu (Q.Z.)
Edited By Vicki Grassian

Abstract

Dark aqueous-phase reactions involving the nitrosation and nitration of aromatic organic compounds play a significant role in the production of light-absorbing organic carbon in the atmosphere. This process constitutes a crucial aspect of tropospheric chemistry and has attracted growing research interest, particularly in understanding the mechanisms governing nighttime reactions between phenols and nitrogen oxides. In this study, we present new findings concerning the rapid dark reactions between phenols containing electron-donating groups and inorganic nitrite in acidic aqueous solutions with pH levels <3.5. This reaction generates a substantial amount of nitroso- and nitro-substituted phenolic compounds, known for their light-absorbing properties and toxicity. In experiments utilizing various substituted phenols, we demonstrate that their reaction rates with nitrite depend on the electron cloud density of the benzene ring, indicative of an electrophilic substitution reaction mechanism. Control experiments and theoretical calculations indicate that the nitrosonium ion (NO^+) is the reactive nitrogen species responsible for undergoing electrophilic reactions with phenolate anions, leading to the formation of nitroso-substituted phenolic compounds. These compounds then undergo partial oxidation to form nitro-substituted phenols through reactions with nitrous acid (HONO) or other oxidants like oxygen. Our findings unveil a novel mechanism for swift atmospheric nitrosation and nitration reactions that occur within acidic cloud droplets or aerosol water, providing valuable insights into the rapid nocturnal formation of nitrogen-containing organic compounds with significant implications for climate dynamics and human health.

Keywords: brown carbon, phenols, nitrosonium ions, fast aqueous-phase dark reaction

Significance Statement

Phenols undergo rapid dark reactions with nitrite and HONO in acidic aqueous solutions, yielding products with notable light-absorbing properties and toxicity. This process is a critical component of nighttime chemistry in the troposphere, yet its underlying mechanism remains unclear. Our study reveals that nitrite can produce a substantial quantity of nitrosonium ions (NO^+) within acidic cloud droplets and aerosols. These ions then react with electron-rich organic compounds in the atmosphere, leading to the formation of various nitroso and nitro compounds. This finding highlights the necessity of reassessing atmospheric aqueous-phase reaction mechanisms involved in the generation of nitrogen-containing organic compounds, which holds significant implications for both climate change and public health.

Introduction

Organic compounds that absorb light, also known as brown carbon (BrC), constitute a crucial component of atmospheric organic aerosols (1). These compounds impact radiative forcing by absorbing sunlight, especially at shorter wavelengths, and by modifying the optical properties of black carbon (2, 3). Moreover, the presence of light-absorbing organic compounds, particularly aromatic compounds, has garnered increasing attention due to their significant environmental and health implications. These compounds are known to contribute to elevated air pollution risks and associated mortality and morbidity (4–6). Global estimates attributed ~7 million deaths to air pollution in 2019 (7–9), underscoring the importance of studying atmospheric chemical processes that contribute to the formation of light-absorbing and toxic organic carbon (10–13).

Atmospheric aqueous-phase reactions play a pivotal role in the generation of secondary species (14–16), with a key outcome being

Competing Interest: The authors declare no competing interests.
Received: April 16, 2024. **Accepted:** August 26, 2024

the formation of light-absorbing organic carbon (1, 17). Nitrogen-containing aromatic compounds, particularly phenols, are the main contributors to chromophores in BrC (18). While numerous studies have investigated aqueous-phase reactions for the production of nitrogen-containing phenols under light irradiation in laboratory settings (19–27), a notable gap remains in our understanding due to limited research conducted under dark conditions typical of nighttime environments.

Kroflič et al. (28) showed that guaiacol (GUA) reacts with sodium nitrite under dark conditions in a solution with a pH of 4.5. However, this reaction proceeded slowly, with ∼20% of GUA remaining unreacted after 24 h. In a follow-up study, quantum chemistry was employed to demonstrate that the potential mechanism of this reaction involves the formation of ·NO and ·NO_2 radicals via the thermal decomposition of HONO. These radicals then react with GUA to yield 4-nitroguaiacol and 6-nitroguaiacol (29). Furthermore, a similar experimental study utilized electrochemical techniques to investigate the potential mechanism of the dark aqueous-phase nitration of 3-methylcatechol by NO_2^- at a higher pH of 6.5 (30). Their results indicate that NO_2^- undergoes an addition reaction with 3-methyl-o-quinone, which is a reactive intermediate, leading to the formation of methyl-nitrocatechol compounds (31).

It is worth noting that most documented dark aqueous-phase reactions were conducted at pH >4.5, while the pH of actual atmospheric aqueous phases can be considerably lower. For example, the pH of clouds and fog water ranges from 2.0 to 7.0, while continental aerosols display a pH range of −1.0 to 5.0. In urban areas, where concentrations of aromatic compounds are elevated due to anthropogenic emissions or biomass burning, aerosols typically maintain a pH <4.0 (32–39). Recently, Wang et al. (40) reported a fast dark aqueous-phase reaction between catechol and nitrite at pH 3.5 that achieved nearly complete catechol conversion within 2 h. However, the specific mechanism underlying the rapid reaction between phenols and nitrite at low pH levels remains unknown.

To address this knowledge gap, we investigated dark aqueous-phase reactions between nitrite and different phenols under acidic atmospheric conditions. Additionally, we conducted quantum chemistry calculations to gain insights into the reactions between phenols and nitrosonium ions (NO^+). Our results reveal that in low-pH aqueous solutions, nitrite mainly exists as the nitrous acidium ion (H_2ONO^+), which converts into NO^+. This reactive species promptly reacts with phenolates in the absence of light, leading to a substantial production of light-absorbing organic carbon.

Results and discussion

Fast aqueous-phase dark reaction of phenols with inorganic N(III) Species

We studied the reactions involving seven different phenols and $NaNO_2$ using the experimental conditions outlined in Table S1, SI Appendix. In aqueous solutions containing nitrite, three inorganic N(III) species may coexist: the nitrous acidium ion (H_2ONO^+), nitrous acid (HONO), and nitrite (NO_2^-) (41–44). The mole fractions of these species are influenced by the pH value of the solution (41).

Figure 1A shows the aqueous reaction kinetics of 0.1 mM GUA and 1 mM $NaNO_2$ in a pH = 3.0 (±0.1) solution under dark conditions with air bubbling. GUA is a common volatile methoxyphenol in the atmosphere, primarily derived from biomass burning (45, 46). In this experimental setup, the reaction between GUA and $NaNO_2$ exhibited first-order kinetics, with a pseudo-first-order rate constant of ∼0.026 min^{-1} and a half-life time of ∼27 min. As a result, ∼89% of the initial GUA was consumed within 1 h. The reaction generated a significant amount of light-absorbing organic carbon, including 4-NGUA (4-nitrosoguaiacol) and 6-NGUA (6-nitrosoguaiacol). This is demonstrated by notable absorption peaks observed at 303, 360, and 480 nm (Fig. 1B). The formation kinetics of 4-NGUA and 6-NGUA, along with the degradation rate of GUA, aligns with the formation rate of the nitro-substituted GUA products (Figs. S2 and S3, SI Appendix).

The kinetics of dark aqueous-phase reactions between GUA and inorganic N(III) species was further examined under varying molar ratios of GUA and $NaNO_2$ that are relevant to atmospheric conditions. Concentrations of methoxyphenols in biomass burning plumes can reach several micrograms per cubic meter (47). Due to their substantial Henry's law constants (48), methoxyphenols readily dissolve in atmospheric aqueous phases, with a total concentration reaching as high as 0.1 mM in fog waters (49–51). Nitrite concentrations in cloud and fog droplets range from 0.01 to 1000 μM (52, 53). As shown in Fig. S4, SI Appendix, when the $NaNO_2$ concentration greatly exceeds that of GUA (at a molar ratio >10:1), the reaction follows pseudo-first-order kinetics, with the rate constant directly proportional to the nitrite concentration. Under these conditions, the GUA decay rate ($R = k_{obs} \times [GUA]_0$) remains constant at ∼0.0026 mM min^{-1} with an initial $NaNO_2$ concentration of 1.0 mM (Fig. S5, SI Appendix). However, when the initial concentrations of GUA and nitrite are comparable, the reaction exhibits second-order kinetics (Fig. S6, SI Appendix).

We further investigated the reaction rates between different substituted phenols and nitrite, using additional phenols commonly found in the atmosphere (45, 46). These phenols encompass those substituted with electron-donating groups, such as creosol, syringol, and eugenol, as well as those with electron-withdrawing groups, such as vanillin, vanillin acid, and syringaldehyde (Fig. S1 and Table S1, SI Appendix). The pseudo-first-order rate constants for the decay of these phenols exhibited a notable increase in the presence of electron-donating groups (Fig. 1C) and conversely decreased with the inclusion of electron-withdrawing groups (Fig. 1D). This observed trend underscores a strong correlation between substituent properties and system reactivity, indicating that the electron cloud density of the benzene ring plays a crucial role in determining the pseudo-first-order rate constant in the dark aqueous-phase reaction between phenols and nitrite under low pH conditions. Specifically, a higher electron cloud density accelerates the reaction rate, while a lower electron cloud density retards it. These findings support an electrophilic substitution mechanism, where an aromatic ring with higher electron density is more susceptible to electrophilic attack by the inorganic N(III) species, resulting in a faster reaction rate.

Potential mechanisms for aqueous reactions of phenols and nitrite at low pH

To elucidate the mechanisms of dark aqueous-phase reaction between phenols with nitrite, we used high-resolution mass spectrometry (HRMS) to analyze the molecular compositions of the reaction products. Figure 2A shows the negative-mode electrospray ionization (ESI) mass spectra (MS) of the solution containing 0.1 mM GUA and 1 mM $NaNO_2$ at pH 3.0 after 30 min in the dark. Alongside the ion corresponding to nitro-GUA at $m/z = 168.0304$ ($C_7H_6NO_4^-$), we also detected an ion representing nitroso-GUA at $m/z = 152.0355$ ($C_7H_6NO_3^-$), which indicate the occurrence of nitroso substitution reaction. In contrast, the reaction between nitrite and vanillin proceeded slowly (Fig. 2B), and analysis of its HRMS

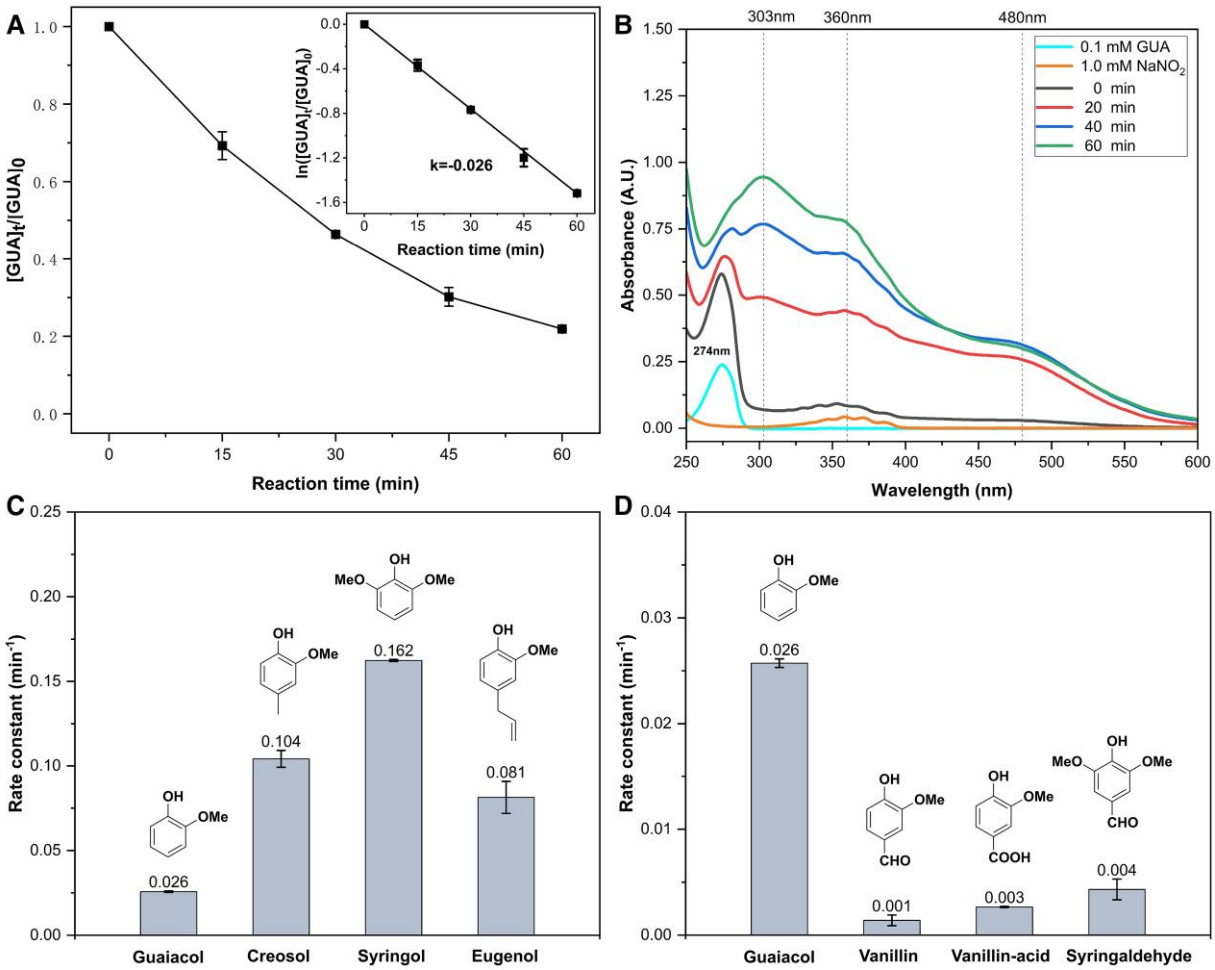

Fig. 1. A) The kinetics of the dark aqueous-phase reaction between GUA and $NaNO_2$, with the inset showing the pseudo-first-order rate constant for the reaction. B) UV–Vis absorption spectra of the reaction solution containing GUA and $NaNO_2$ at different time points during the reaction. C) and D) Pseudo-first-order rate constants for various substituted GUAs undergoing dark aqueous reactions with $NaNO_2$. Experimental conditions: [phenols] = 0.1 mM, [$NaNO_2$] = 1 mM, pH = 3.0 ± 0.1, with zero air bubbling, room temperature.

data did not reveal ions indicative of nitroso-substituted vanillin. Instead, only nitro-substituted vanillin ions (e.g. $C_8H_6NO_5^-$ at m/z = 196.0252) were identified. These findings suggest that the rapid reactions observed for electron-rich phenols with nitrite in acidic aqueous environments were primarily facilitated by the nitrosation pathway.

The reaction mechanism between phenols and nitrite in the aqueous phase is known to occur under two distinct conditions. One of them involves an addition reaction that takes place at pH above 5.5, where NO_2^- is the predominant reactive nitrogen species (RNS) driving the reaction (30, 31). As illustrated in Fig. S7A, SI Appendix, for catechol, upon oxidation by HONO, the catechol molecule releases two hydrogens and two electrons, forming diquinone as an intermediate product. Subsequently, diquinone undergoes an addition reaction with NO_2^-, leading to the formation of nitro-substituted products. The other mechanism involves radical reactions occurring at pH levels <5.5, where the ·NO radical and $\cdot NO_2$ radical, generated through the thermal decomposition or oxidation of HONO, act as the main RNS that interact with phenols (28, 29, 54–57). Within this solution, phenols (Ar–OH) undergo hydrogen-atom abstraction by free radicals (e.g. ·OH, ·NO, and $\cdot NO_2$) to form corresponding phenoxy radicals (Ar–O), which subsequently isomerize into aryl radicals (·Ar–OH). These ·Ar–OH radicals then react with ·NO and $\cdot NO_2$ to yield nitro-substituted and nitroso-substituted products, respectively (Fig. S7B, SI Appendix).

In this study, we discovered that although the reactions between phenols and nitrite in solutions with pH levels >3.5 align with these mechanisms, they do not fully explain the experimental observations at pH < 3.5. This is particularly evident in comparing the reaction rates of different phenols. For example, the pseudo-first-order reaction rate between GUA and nitrite was ~26 times faster than that between vanillin and nitrite (Fig. 1D), indicating a pronounced dependence of the reaction rate on the electron cloud density of the benzene ring. However, considering our earlier observation of a rapid reaction between vanillin and the $\cdot NO_2$ radical at pH 3.0 (20), the presence of electron-withdrawing functional groups on the benzene ring did not significantly reduce the nitration rate of phenols. Thus, it appears that that the nitrosation process, rather than nitration, is considerably affected by the electron density of the benzene ring. This conclusion is further supported by the absence of nitroso-vanillin in the reaction products of vanillin and nitrite as determined through HRMS analysis.

Here, we propose a novel mechanism suggesting that the reaction between phenols and nitrite at pH < 3.5 proceeds through the interaction of phenols with NO^+. In aqueous solutions, nitrite can exist in three forms—H_2ONO^+, HONO, and NO_2^- (41–44). The pKa

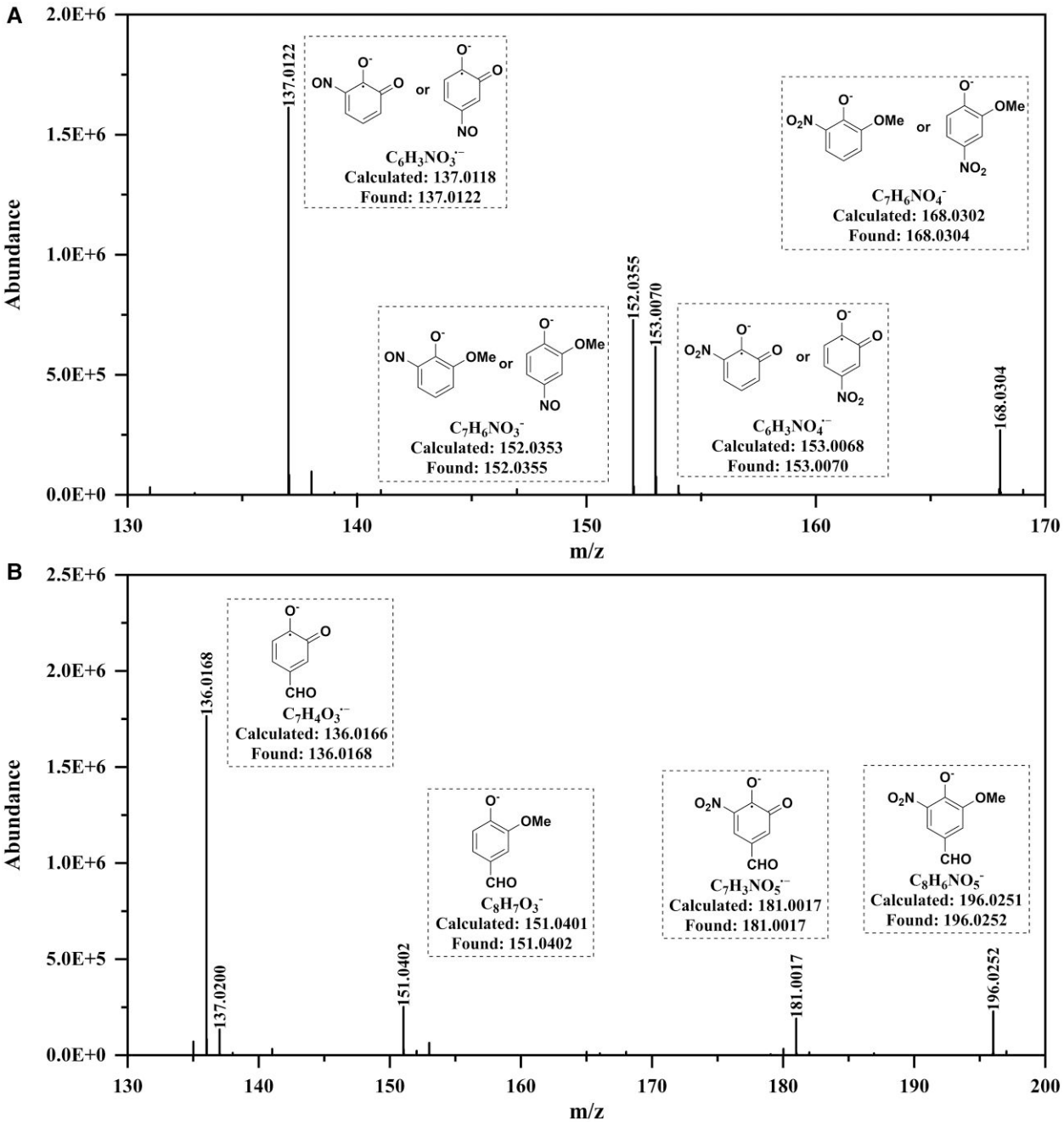

Fig. 2. The HRMS of the reaction products of phenolic compounds and $NaNO_2$. A) GUA. B) Vanillin. Experimental conditions: [phenols] = 0.1 mM, [$NaNO_2$] = 1 mM, pH = 3.0 ± 0.1, zero air bubbling, room temperature.

values for H_2ONO^+ and HONO are 1.7 and 2.8, respectively (41). As illustrated in the distribution curves of these N(III) species relative to pH (Fig. S8, SI Appendix), H_2ONO^+ dominates with mole fractions exceeding 0.8 at pH <1.0. However, at pH > 3.5, H_2ONO^+ is depleted, and NO_2^- and HONO become the predominant forms. As the pH drops below 3.5, the proportion of H_2ONO^+ increases, facilitating the release of NO^+ by H_2ONO^+.

To further explore this mechanism and gain insights into the key role of NO^+, we conducted quantum chemistry calculations to probe the reactions between NO^+ and three phenols: GUA, vanillin (consisting of a GUA moiety with an electron-withdrawing aldehyde functional group linked to the ring), and creosol (containing a GUA moiety with an electron-donating methyl functional group attached to the ring).

In a previous report, the reaction mechanism between GUA and NO^+ was meticulously investigated, yet no plausible transition state (TS) could be identified (29). Similarly, our investigation into the reaction mechanisms of NO^+ with vanillin and creosol also failed to yield viable TSs. Details regarding TS calculations and the calculated energy barriers for the reactions are given in Section S1 and Figs. S9 and S10, SI Appendix. In essence, these findings indicate that there are no discernable reactions between NO^+ and GUA, vanillin, and creosol in their molecular forms.

However, as illustrated in Fig. 3A and B, the activation energies for the reactions of the anions of GUA ($C_7H_7O_2^-$) and creosol ($C_8H_9O_2^-$) with NO^+ are notably low (5.2, 1.7, and 2.3 kcal/mol, respectively), indicating the potential for rapid electrophilic substitution reactions between NO^+ and GUA and creosol. The

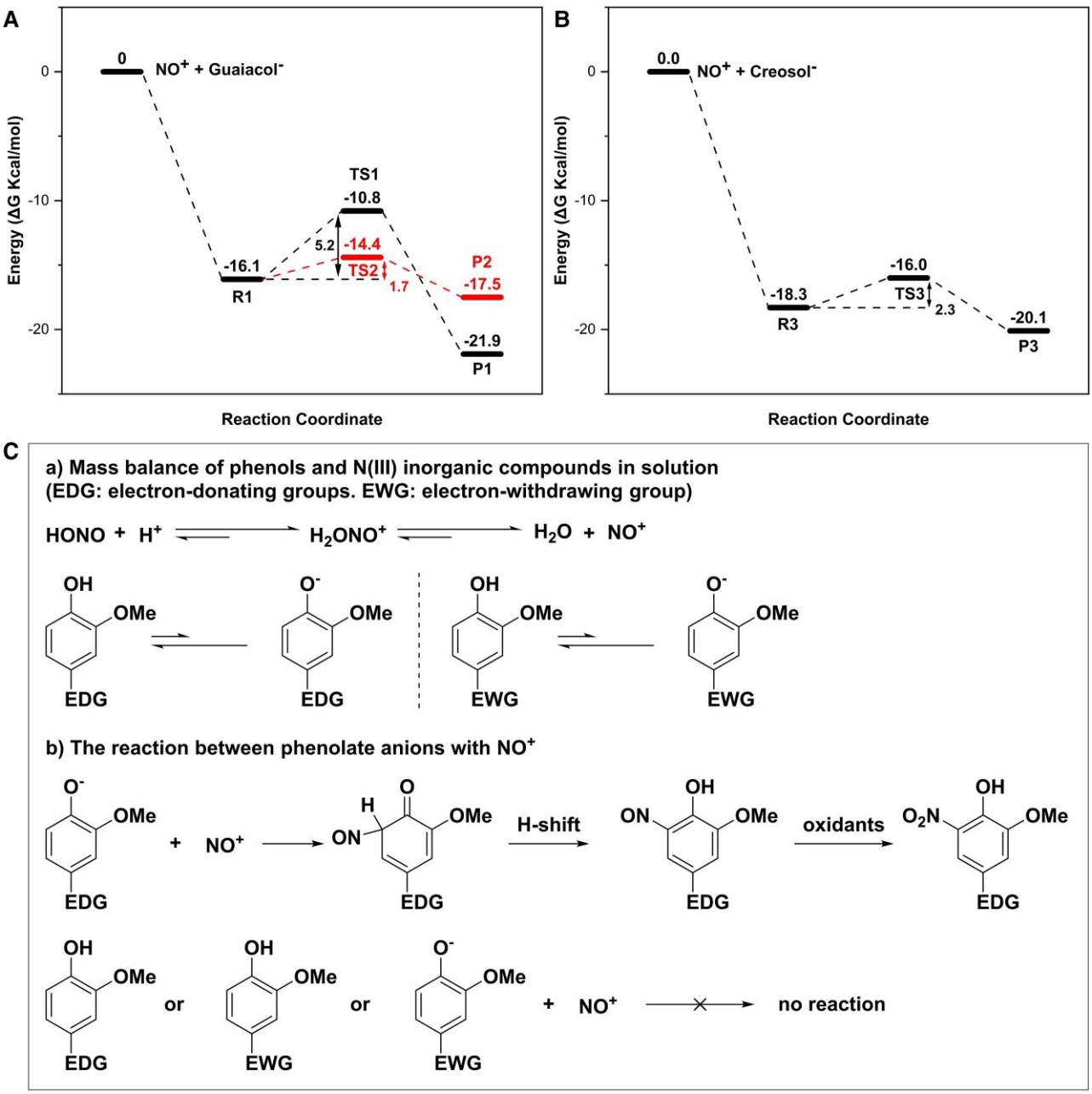

Fig. 3. Gibbs free energy (in kcal/mol at 298.15 K) profiles for the reaction of phenolic compounds and NO^+ at the DLPNO-CCSD(T)/aug-cc-pVTZ/SMD(water)//B3LYP-D3(BJ)/aug-cc-pVTZ/SMD(water) level of theory with the zero-point energy correction applied. A) GUA, the black line represents the reaction mechanisms for forming 4-NGUA and the red line represents the reaction mechanisms for forming 6-NGUA, B) Creosol. C) The new reaction mechanism of phenols and N(III) inorganic compounds. The molecular configurations along the reaction coordinates in A) and B) are presented in Fig. S9.

molecular structures of the reaction intermediates and products are presented in Fig. S11, SI Appendix. In contrast, no viable TS has been identified for the vanillin system ($C_8H_7O_3^-$) (Section S1 and Fig. S10D, SI Appendix), which is consistent with the slow reaction observed in the experiment involving vanillin and $NaNO_2$ at pH 3.0 (Fig. 1D). These results, coupled with the lack of nitroso-vanillin as a reaction product, indicate that phenols with electron-withdrawing groups are not prone to rapid reactions with NO^+.

Figure 3C summarizes the novel reaction mechanism we propose for dark aqueous reactions involving phenols and N(III) species at pH < 3.5. The initial step of this mechanism involves the release of NO^+ from H_2ONO^+, which is the primary form of the N(III) species under low pH conditions. It subsequently undergoes an electrophilic substitution reaction with the phenolate anions ($Ar–O^-$), leading to the formation of nitroso-substituted products. These products are then partially oxidized to nitro-substituted products by HONO or other oxidants, such as oxygen (Fig. 3C). Our experimental findings and theoretical calculations indicate that this reaction pathway is slow for phenols containing electron-withdrawing groups, even under low pH conditions. This observation aligns with previously reported mechanisms (28–31).

In this newly proposed mechanism, the reaction rate is influenced by two factors: (i) the concentrations of NO^+ and the phenolate anion and (ii) the activation energy associated with the

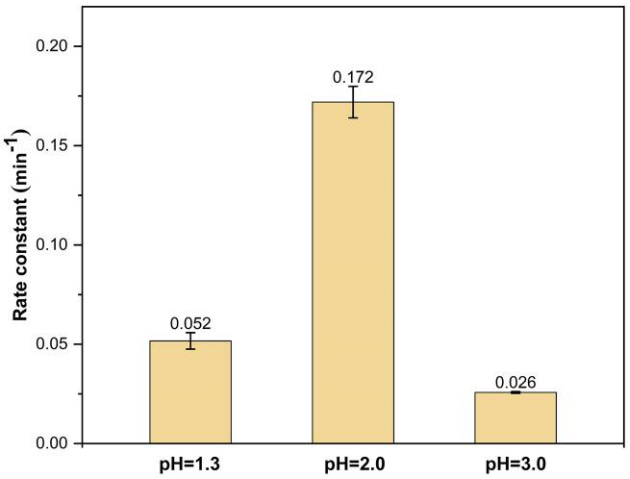

Fig. 4. Effect of acidic conditions (pH < 3.0) on the pseudo-first-order rate constants of dark aqueous-phase reactions involving GUA and $NaNO_2$. Experimental conditions: [GUA] = 0.1 mM, [$NaNO_2$] = 1 mM, and zero air bubbling.

reaction between NO^+ and the phenolate anion. In theory, as the pH value decreases <3.0, the concentration of NO^+ is expected to rise (Fig. S8, SI Appendix), while the concentration of the phenolate anion is anticipated to decrease. This intricate balance could lead to a rate constant that initially rises and then declines with decreasing pH values. This theoretical prediction is supported by the observed variations in the pseudo-first-order rate constants of GUA and $NaNO_2$ at pH values of 1.3, 2.0, and 3.0, where $k_{pH=2.0} > k_{pH=1.3} > k_{pH=3.0}$ (Fig. 4).

We further demonstrate the applicability of this mechanism in predicting dark aqueous-phase reactions involving other phenols and nitrite, as it not only explains the rapid dark aqueous-phase reactions of methoxyphenol and nitrite but also sheds light on the fast reaction between diphenol (catechol) and nitrite (40). As illustrated in Fig. S10, SI Appendix, after a proton loss from catechol, the resulting catechol anion can react with NO^+ with low activation energies of 4.3 and 1.3 Kcal/mol (Fig. S13, SI Appendix, structures of the intermediates and products are presented in Fig. S14, SI Appendix). Furthermore, Figs. S5–S17, SI Appendix, depict the TSs and activation energies for the reaction between 4-chloro-2-methoxyphenol (4ClGUA) and NO^+, predicting that 4ClGUA can rapidly react with nitrite in the dark aqueous phase despite the weak electron-withdrawing nature of the chlorine atom. Our subsequent experiments confirmed this prediction, showing a pseudo-first-order rate constant of ~0.028 min^{-1} and a half-life time of ~25 min for the reaction between 4ClGUA and nitrite (Fig. S18, SI Appendix).

Effects of atmospheric conditions

To assess the reaction rates of phenols with nitrite under different atmospheric conditions, we conducted a series of control experiments using GUA and $NaNO_2$ as a model reaction system (Table S1, SI Appendix). We studied the influence of solution pH, recognizing its pivotal role in tropospheric aqueous-phase chemistry, which includes its influences on processes such as gas–liquid-phase partitioning and ion speciation of dissolved compounds (35, 36). The dark reaction between GUA and $NaNO_2$ exhibited rapid kinetics at pH values <3.5, with half-lives of <58 min, while the reactivity greatly decreased above a pH of 4.0 (Fig. 5A). Additionally, a temperature-dependent relationship was evident, with higher

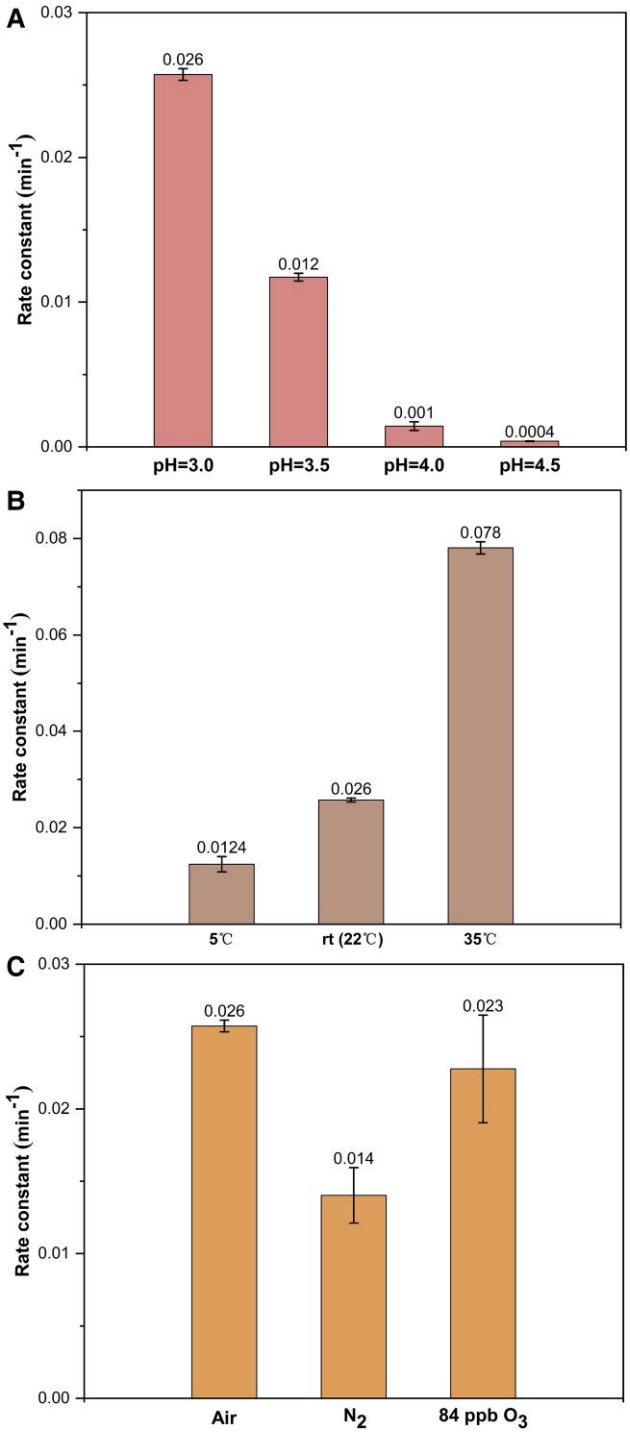

Fig. 5. Dark aqueous-phase reaction rates of GUA and $NaNO_2$ under various atmospheric conditions: A) Different pH values. B) Different temperatures. C) Different air bubbling. Experimental conditions: [GUA] = 0.1 mM, [$NaNO_2$] = 1 mM, pH = 3.0 ± 0.1 (unless explicitly stated), with zero air bubbling (unless explicitly stated).

temperatures markedly accelerating the reaction rate (Fig. 5B). These findings indicate that rapid dark aqueous-phase reactions of phenols and nitrite are more likely to occur under conditions of elevated temperature and low pH.

Figure 5C shows that the dark aqueous reactions of GUA and $NaNO_2$ are facilitated by the presence of dissolved oxygen. In our experiments, we simulated an anoxic environment similar to the upper atmosphere by bubbling inert gas (N_2) through the solution.

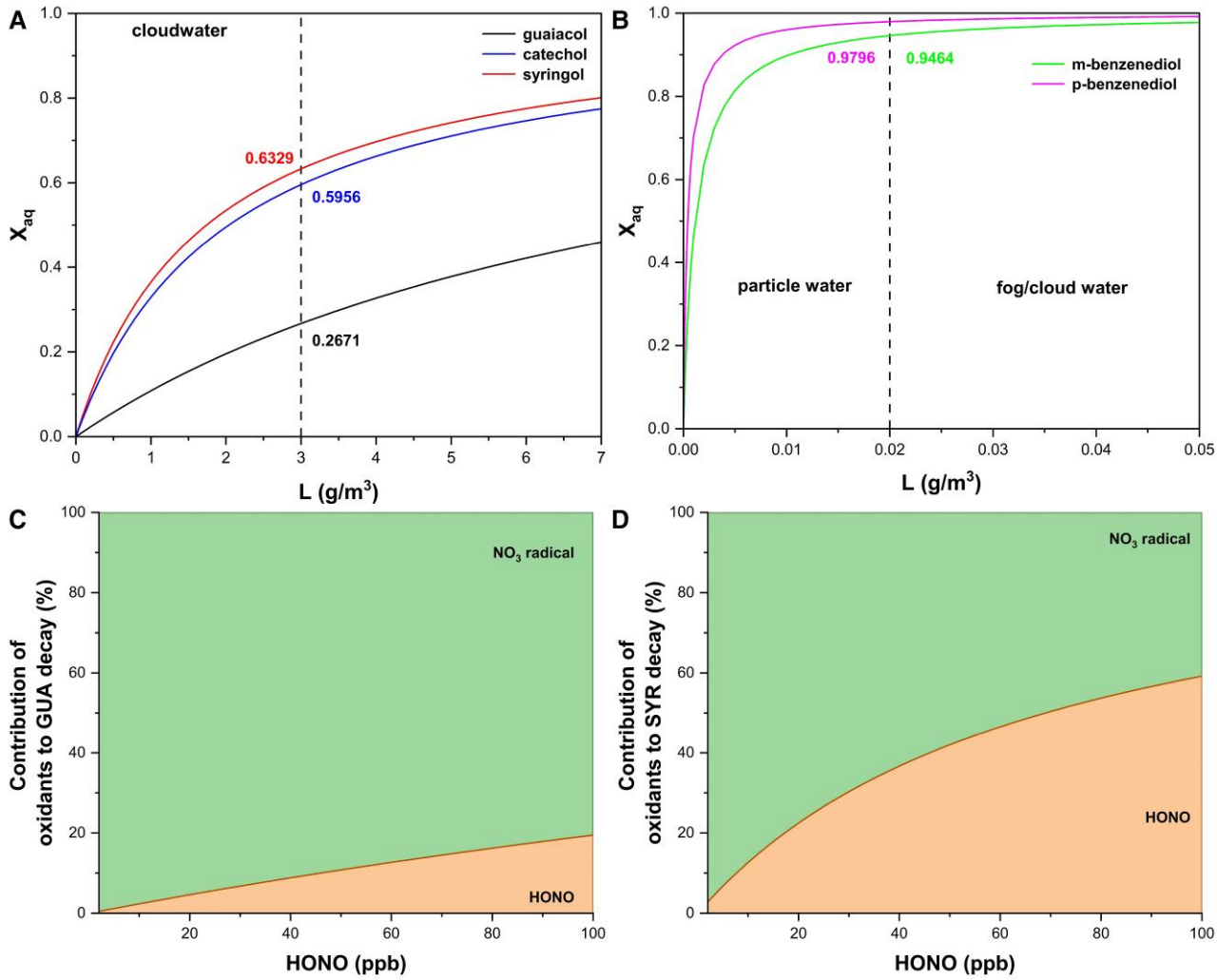

Fig. 6. The gas–water distribution of different phenolic compounds under an air temperature of 5 °C and varying LWCs: A) compounds with lower Henry's law constants (<10^6 m atm^{-1}) and B) compounds with Henry's law constants (>10^6 m atm^{-1}). The percent contributions of NO_3 radicals and HONO to the degradation of GUA (C) and syringol (D) as a function of HONO gas-phase concentrations ($[HONO]_g$) at an aqueous-phase pH = 3.0.

Under anoxic conditions, we observed a pseudo-first-order rate constant of ~0.014 min^{-1} and a half-life of ~50 min at pH = 3.0, which are nearly 50% slower than the rates observed under air-saturated conditions. However, elevated ozone concentration was found to have minimal effects on the reaction rate. Specifically, we observed a rate constant of ~0.023 min^{-1} and a half-life of ~30 min at an ozone concentration of 84 ppb, which were similar to those in air-saturated solutions. This suggests that ozone concentration within typical ambient levels does not significantly impact the reaction rate.

Implications

Inorganic N(III) species are frequently detected in atmospheric cloud droplets and aerosols, existing in diverse forms across a wide range of pH values. This diversity influences their chemical properties and underscores their significance as sources of RNS. Chemical interactions between VOCs and RNS components can potentially lead to the formation of nitroso and nitro compounds, which have strong light-absorbing properties and contribute to the complex chemistry and radiative forcing within the atmosphere. Additionally, nitro and nitroso compounds are associated with considerable toxicity.

In cloud droplets and aerosol particles, light-absorbing material primarily originates from secondary formation processes and biomass burning, which collectively contribute to 67–85% of the total BrC content (17). Phenolic compounds are significant products of biomass burning, with global emissions estimated at 4.7 Tg per year (45, 46). Due to their varying substitution structures, the Henry's law constants for these compounds range from 4×10^1 to 3.1×10^8 M atm^{-1} (48). We selected GUA, catechol, syringol, m-benzenediol, and p-benzenediol to model gas–water distribution (Section S3, SI Appendix). Our simulations indicate that for phenols with lower Henry's law constants (<10^6 M atm^{-1}), up to 60% of syringol and catechol, and about 26% for GUA, may partition into the cloud water phase under the liquid water content (LWC) condition of 3 g m^{-3} (Fig. 6A). Conversely, for phenols with a high Henry's law constant (>10^6 M atm^{-1}), nearly all of the compounds partition into the aqueous phase under fog/cloud conditions (e.g. LWC > 0.02 g m^{-3}), and a significant proportion of these compounds distribute into the aerosol water phase even when LWC is as low as a few μg m^{-3} (Fig. 6B).

During the daytime, photochemical oxidation of phenolic compounds in the aqueous phase, primarily driven by OH radicals, singlet oxygen ($^1O_2$*), and triplet carbonyls (^{3}C*) (58, 59), is an important source of secondary organic aerosol (60). In the presence

of inorganic N(III) species, additional RNS like ·NO and ·NO_2 are generated, which can react with phenolic compounds to form light-absorbing substances (20, 25, 27).

The significant role of aqueous-phase secondary processes in accelerating the formation of light-absorbing substances has been observed during nighttime as well (61). However, previous experimental studies have indicated that the dark aqueous-phase formation of nitrophenols occurs slowly (28, 30). In this study, we have identified a fast reaction mechanism between nitrite and phenols within the dark aqueous solution under conditions relevant to the atmosphere. This discovery may shed light on the rapid formation of BrC observed during nighttime. It represents a noteworthy reaction mechanism, particularly relevant in regions where the pH of atmospheric water droplets and aerosols has shown a trend of persistent decline (37, 39).

At nighttime, the degradation of phenols is primarily driven by NO_3 radicals and HONO (62, 63). Field observations of nighttime biomass burning plumes reveal high HONO concentrations, potentially reaching up to 100 ppb (40). In contrast, NO_3 concentrations are relatively low (<3 ppt), with NO_3 primarily reacting with NO_2 to form N_2O_5 and engaging in gas-phase reactions with biomass burning volatile organic compounds (64). To better understand the contributions of HONO and NO_3 radicals to the aqueous-phase degradation of phenolic compounds at nighttime, we employed a box model (Section S3, SI Appendix). The typical nighttime concentration of NO_3 radicals in cloud droplets is around 10^{-12} M (62), while HONO concentrations in the aqueous phase depend directly on its gas-phase levels. We simulated gas-phase HONO concentrations ranging from 0 to 100 pb. Our results show that at 100 ppb $[HONO]_g$, ~20% of GUA is degraded by aqueous-phase HONO at pH 3.0 (Fig. 6C), while for syringol, this figure rises to 59% (Fig. 6D). For other electron-rich phenolic compounds, the proportion of aqueous-phase degradation driven by HONO could be even higher. These findings underscore the critical role of HONO in the nighttime degradation of phenolic compounds and highlight the importance of considering this pathway in atmospheric chemistry models.

It is also important to note that the core RNS (NO^+) identified in this reaction mechanism could participate in reactions with other nucleophilic compounds present in the atmosphere, such as amines. These reactions might lead to the generation of nitrosamines and related toxic compounds, posing significant implications for human health. Future studies on atmospheric aqueous-phase reactions may need to focus on enhancing our understanding of the chemical behavior of inorganic N(III) species under acidic conditions. This knowledge is crucial for unraveling the complexity of atmospheric chemistry and its wide-ranging impacts on the environment and human health. Specifically, further investigation into the mechanisms and kinetics of dark aqueous-phase reactions involving inorganic N(III) species under low pH conditions will provide valuable insights into the formation of secondary N-containing organic compounds and their potential impacts on air quality, climate, and public health. Moreover, such research can aid in the development of targeted strategies aimed at mitigating the impacts of these reactions on atmospheric composition and chemistry.

Materials and methods

Materials

Organic reagents used in this study are outlined in Fig. S1, SI Appendix. GUA (99%), 4ClGUA (98%), Na_2SO_4 (>99%), and $NaNO_2$ (>99%) were purchased from Macklin. Vanillin acid (98%), eugenol (98%), syringaldehyde (98%), creosol (98%), and syringol (98%) were purchased from Meryer. Vanillin (98%) was purchased from Aladdin.

Characterization methods

HPLC analysis

The concentration of the precursors was determined using an HPLC (Thermo Scientific UltiMate 3000) equipped with a diode array detector and an Agilent 5 TC-C18 column (150 × 4.60 mm, 5 μm). The column temperature was maintained at 25 °C, and the flow rate was set to 1 mL/min. Detection was performed at a wavelength of 274 nm. To analyze GUA, eugenol, syringol, creosol, and 4ClGUA , the mobile phase consisted of 60/40 (v/v) acetonitrile/water acidified with trifluoroacetic acid (TFA, 0.1%). To analyze vanillin, vanillin acid, and syringaldehyde, the mobile phase consisted of 50/50 (v/v) methanol/water acidified with TFA (0.1%).

Direct infusion HRMS

The reaction solution was filtered through the filter membrane and then directly introduced into the Agilent 6546 quadrupole time-of-flight mass spectrometer (QTOF-MS, Santa Clara, CA, USA) with ESI source in negative mode. The MS parameters were applied as follows: nebulizer, 25 psi; gas flow, 10 L/min; sheath gas temperature, 330 °C; capillary voltage, 3,500 V; and sheath gas flow, 12 L/min. The MS fragmentation data were collected in the 90–500 m/z range. MassHunter Qualitative and Quantitative software version 10.0 was used for data analysis.

UV–Vis spectroscopy

An ultraviolet–visible spectrophotometer (Youke, T2602, Shanghai, China) was used to monitor the absorption of GUA during its reactions with $NaNO_2$ and to determine the spectrum of samples in 300–600 nm. The reaction solution was directly loaded into the instrument before irradiation without any alterations. Spectra of the GUA—$NaNO_2$ reaction were collected every 20 min for 1 h.

Dark bulk aqueous experiment

All experiments were performed in a 250-mL airtight Pyrex tube which was wrapped in aluminum foil equipped with a magnetic stirrer and a bubble tube for feeding high-purity zero air or nitrogen. A 200-mL reaction solution of the organic compound and $NaNO_2$ with other reactants was prepared. The pH of the reaction solution was regulated by H_2SO_4 and NaOH. The pH of solutions was measured with a pH meter/redox potentiometer/conductivity meter (AZ-86555) that was calibrated with commercial pH standards. Aliquots of 10 mL reaction solution, to which 200 μL of 1 M NaOH aqueous solution was added to stop the reaction, were sampled for chemical analysis every 15 min for 1 h. Each experiment was repeated at least twice.

Quantum chemistry calculations

Geometry optimizations for all molecular structures of the reactants, products, and TSs were using the B3LYP-D3(BJ) (65, 66) (B3LYP with the GD3BJ dispersion correction) functional with the aug-cc-pVTZ basis set (67) using the SMD solution model to calculate solvent effects in water (68) with Gaussian 16 package (69). Optimized structures were verified by frequency computations as minima (zero imaginary frequencies) or transition structures (a single imaginary frequency). Intrinsic reaction coordinate calculations were performed to ensure that the first-order saddle points found were true TSs connecting the reactants and the products. Single-point energies and solvent effects in water were calculated at DLPNO-CCSD(T)/aug-cc-pVTZ (70–75) level of theory

based on the optimized geometries at the B3LYP-D3(BJ)/aug-cc-pVTZ using the SMD solvation model with the ZPE correction employed which using the ORCA 5.0.3 program package (76). The Multiwfn 3.8 (77) and Shermo 2.4 (78) were used for data analysis.

Supplementary Material

Supplementary material is available at *PNAS Nexus* online.

Funding

This work was supported by the Shenzhen Key Laboratory of Precision Measurement and Early Warning Technology for Urban Environmental Health Risks (ZDSYS20220606100604008), Guangdong Provincial Observation and Research Station for Coastal Atmosphere and Climate of the Greater Bay Area (2021B1212050024), and Shenzhen Science and Technology Program (KQTD20210811090048025, KCXFZ20230731093601003). Q.Z. acknowledges the support from the U.S. National Science Foundation under grant number AGS-2308645.

Author Contributions

B.C. and X.Y. designed the research; B.C., Y.W., and X.Y. performed the research; B.C., Y.L., J.Y., J.Z., Y.Z., L.Z., T.-M.F., Q.Z., and X.Y. analyzed the data; and B.C., Y.W., Q.Z., and X.Y. wrote the paper.

Data Availability

The data that support the findings of this study are available in the supplementary material of this article.

References

1 Laskin A, Laskin J, Nizkorodov SA. 2015. Chemistry of atmospheric brown carbon. *Chem Rev*. 115:4335–4382.
2 Stevenson DS, *et al.* 2013. Tropospheric ozone changes, radiative forcing and attribution to emissions in the Atmospheric Chemistry and Climate Model Intercomparison Project (ACCMIP). *Atmos Chem Phys*. 13:3063–3085.
3 Zhang Y, *et al.* 2017. Top-of-atmosphere radiative forcing affected by brown carbon in the upper troposphere. *Nat Geosci*. 10:486–489.
4 ATSDR. 2023. *Toxicological profile for nitrophenols*. U.S Department of Health and Human Services.
5 von Schneidemesser E, *et al.* 2015. Chemistry and the linkages between air quality and climate change. *Chem Rev*. 115:3856–3897.
6 Zhang Q, *et al.* 2023. Nitroaromatic compounds from secondary nitrate formation and biomass burning are Major proinflammatory components in organic aerosols in Guangzhou: a bioassay combining high-resolution mass spectrometry analysis. *Environ Sci Technol*. 57:21570–21580.
7 Perring AE, Pusede SE, Cohen RC. 2013. An observational perspective on the atmospheric impacts of alkyl and multifunctional nitrates on ozone and secondary organic aerosol. *Chem Rev*. 113:5848–5870.
8 Zhang Q, *et al.* 2022. Overview of particulate air pollution and human health in China: evidence, challenges, and opportunities. *Innovation*. 3:100312.
9 Fuller R, *et al.* 2022. Pollution and health: a progress update. *Lancet Planet Health*. 6:e535–e547.
10 Yan J, Wang X, Gong P, Wang C, Cong Z. 2018. Review of brown carbon aerosols: recent progress and perspectives. *Sci Total Environ*. 634:1475–1485.
11 Al-Abadleh HA. 2021. Aging of atmospheric aerosols and the role of iron in catalyzing brown carbon formation. *Environ Sci Atmos*. 1:297–345.
12 Wang Q, *et al.* 2022. Review of brown carbon aerosols in China: pollution level, optical properties, and emissions. *J Geophys Res Atmos*. 127:e2021JD035473.
13 Li Y, *et al.* 2023. Dissecting the contributions of organic nitrogen aerosols to global atmospheric nitrogen deposition and implications for ecosystems. *Natl Sci Rev*. 10:nwad244.
14 Herrmann H. 2003. Kinetics of aqueous phase reactions relevant for atmospheric chemistry. *Chem Rev*. 103:4691–4716.
15 Ervens B, Turpin BJ, Weber RJ. 2011. Secondary organic aerosol formation in cloud droplets and aqueous particles (aqSOA): a review of laboratory, field and model studies. *Atmos Chem Phys*. 11:11069–11102.
16 Herrmann H, *et al.* 2015. Tropospheric aqueous-phase chemistry: kinetics, mechanisms, and its coupling to a changing gas phase. *Chem Rev*. 115:4259–4334.
17 Guo Z, *et al.* 2022. The optical properties and in-situ observational evidence for the formation of brown carbon in clouds. *Atmos Chem Phys*. 22:4827–4839.
18 Gong Y, *et al.* 2023. Measurement report: brown carbon aerosol in polluted urban air of north China plain: day-night differences in the chromophores and optical properties. *Atmos Chem Phys*. 2023:15197–15207.
19 Ma J, *et al.* 2017. Photochemical reaction between triclosan and nitrous acid in the atmospheric aqueous environment. *Atmos Environ*. 157:38–48.
20 Pang H, *et al.* 2019. Nitrite-Mediated photooxidation of vanillin in the atmospheric aqueous phase. *Environ Sci Technol*. 53:14253–14263.
21 Lu J, *et al.* 2019. Photochemical reaction kinetics and mechanistic investigations of nitrous acid with sulfamethazine in tropospheric water. *Environ Sci Pollut Res*. 26:26134–26145.
22 Anglada JM, Martins-Costa MTC, Francisco JS, Ruiz-López MF. 2020. Photoinduced oxidation reactions at the air–water interface. *J Am Chem Soc*. 142:16140–16155.
23 Otero V, *et al.* 2020. A little key to oxalate formation in oil paints: protective patina or chemical reactor? *Photochem Photobiol Sci*. 17:266–270.
24 Bianco A, Passananti M, Brigante M, Mailhot G. 2020. Photochemistry of the cloud aqueous phase: a review. *Molecules*. 25:423.
25 Mabato BRG, *et al.* 2022. Aqueous secondary organic aerosol formation from the direct photosensitized oxidation of vanillin in the absence and presence of ammonium nitrate. *Atmos Chem Phys*. 22:273–293.
26 Gen M, Liang Z, Zhang R, Go Mabato BR, Chan CK. 2022. Particulate nitrate photolysis in the atmosphere. *Environ Sci Atmos*. 2:111–127.
27 Carena L, *et al.* 2023. Phototransformation of vanillin in artificial snow by direct photolysis and mediated by nitrite. *Environ Sci Technol*. 57:8785–8795.
28 Kroflič A, Grilc M, Grgić I. 2015. Unraveling pathways of guaiacol nitration in atmospheric waters: nitrite, a source of reactive nitronium ion in the atmosphere. *Environ Sci Technol*. 49:9150–9158.
29 Kroflič A, Huš M, Grilc M, Grgić I. 2018. Underappreciated and complex role of nitrous acid in aromatic nitration under mild environmental conditions: the case of activated methoxyphenols. *Environ Sci Technol*. 52:13756–13765.

30 Vidović K, Lašič Jurković D, Šala M, Kroflič A, Grgić I. 2018. Nighttime aqueous-phase formation of nitrocatechols in the atmospheric condensed phase. *Environ Sci Technol*. 52:9722–9730.
31 Vidović K, Kroflič A, Jovanovič P, Šala M, Grgić I. 2019. Electrochemistry as a tool for studies of complex reaction mechanisms: the case of the atmospheric aqueous-phase aging of catechols. *Environ Sci Technol*. 53:11195–11203.
32 Zhang Q, Jimenez JL, Worsnop DR, Canagaratna M. 2007. A case study of urban particle acidity and its influence on secondary organic aerosol. *Environ Sci Technol*. 41:3213–3219.
33 Parworth CL, *et al*. 2017. Wintertime water-soluble aerosol composition and particle water content in Fresno, California. *J Geophys Res Atmos*. 122:3155–3170.
34 Zheng G, *et al*. 2020. Multiphase buffer theory explains contrasts in atmospheric aerosol acidity. *Science*. 369:1374–1377.
35 Pye HOT, *et al*. 2020. The acidity of atmospheric particles and clouds. *Atmos Chem Phys*. 20:4809–4888.
36 Tilgner A, *et al*. 2021. Acidity and the multiphase chemistry of atmospheric aqueous particles and clouds. *Atmos Chem Phys*. 21: 13483–13536.
37 Zhou M, *et al*. 2022. Long-term trends and drivers of aerosol pH in eastern China. *Atmos Chem Phys*. 22:13833–13844.
38 Zheng M, Xu K, Yuan L, Chen N, Cao M. 2022. Fine particle pH and its impact on $PM_{2.5}$ control in a megacity of Central China. *Aerosol Air Qual Res*. 22:210394.
39 Wang G, *et al*. 2022. Quantitative decomposition of influencing factors to aerosol pH variation over the coasts of the South China Sea, East China Sea, and Bohai Sea. *Environ Sci Technol Lett*. 9:815–821.
40 Wang Y, Jorga S, Abbatt J. 2023. Nitration of phenols by reaction with aqueous nitrite: a pathway for the formation of atmospheric brown carbon. *ACS Earth Space Chem*. 7:632–641.
41 Anastasio C, Chu L. 2009. Photochemistry of nitrous acid (HONO) and nitrous acidium Ion (H_2ONO^+) in aqueous solution and ice. *Environ Sci Technol*. 43:1108–1114.
42 Hutchings JW, Ervens B, Straub D, Herckes P. 2010. N-Nitrosodimethylamine occurrence, formation and cycling in clouds and fogs. *Environ Sci Technol*. 44:8128–8133.
43 Donaldson MA, Bish DL, Raff JD. 2014. Soil surface acidity plays a determining role in the atmospheric-terrestrial exchange of nitrous acid. *Proc Natl Acad Sci U S A*. 111:18472–18477.
44 Lei Y, *et al*. 2018. Photochemical reaction kinetics and mechanisms of diethyl phthalate with N (III) in the atmospheric aqueous environment. *J Photochem Photobiol A Chem*. 362:21–30.
45 Liu C, Chen D, Chen X. 2022. Atmospheric reactivity of methoxyphenols: a review. *Environ Sci Technol*. 56:2897–2916.
46 Li F, *et al*. 2023. Aqueous-phase chemistry of atmospheric phenolic compounds: a critical review of laboratory studies. *Sci Total Environ*. 856:158895.
47 Simpson CD, Paulsen M, Dills RL, Liu LJ, Kalman DA. 2005. Determination of methoxyphenols in ambient atmospheric particulate matter: tracers for wood combustion. *Environ Sci Technol*. 39:631–637.
48 McFall AS, Johnson AW, Anastasio C. 2020. Air–water partitioning of biomass-burning phenols and the effects of temperature and salinity. *Environ Sci Technol*. 54:3823–3830.
49 Sagebiel JC, Seiber JN. 1993. Studies on the occurrence and distribution of wood smoke marker compounds in foggy atmospheres. *Environ Toxicol Chem*. 12:813–822.
50 Jaber S, *et al*. 2020. Biodegradation of phenol and catechol in cloud water: comparison to chemical oxidation in the atmospheric multiphase system. *Atmos Chem Phys*. 20:4987–4997.
51 Li M, *et al*. 2020. Nitrated phenols and the phenolic precursors in the atmosphere in urban Jinan, China. *Sci Total Environ*. 714: 136760.
52 Lammel G, Cape JN. 1996. Nitrous acid and nitrite in the atmosphere. *Chem Soc Rev*. 25:361–369.
53 Cui L, Wang S. 2021. Mapping the daily nitrous acid (HONO) concentrations across China during 2006–2017 through ensemble machine-learning algorithm. *Sci Total Environ*. 785:147325.
54 Vione D, *et al*. 2003. New processes in the environmental chemistry of nitrite. 2. The role of hydrogen peroxide. *Environ Sci Technol*. 37:4635–4641.
55 Vione D, Maurino V, Minero C, Pelizzetti E. 2005. Aqueous atmospheric chemistry: formation of 2,4-dinitrophenol upon nitration of 2-nitrophenol and 4-nitrophenol in solution. *Environ Sci Technol*. 39:7921–7931.
56 Ji Y, *et al*. 2017. The role of nitrite in sulfate radical-based degradation of phenolic compounds: an unexpected nitration process relevant to groundwater remediation by in-situ chemical oxidation (ISCO). *Water Res*. 123:249–257.
57 Zhao X, *et al*. 2023. Influence of nitrite on ultraviolet-activated peroxydisulfate degradation of 2,4-dichlorophenol. *ACS EST Engg*. 3:2008–2015.
58 Ma L, *et al*. 2021. Kinetics and mass yields of aqueous secondary organic aerosol from highly substituted phenols reacting with a triplet excited state. *Environ Sci Technol*. 55:5772–5781.
59 Smith JD, Sio V, Yu L, Zhang Q, Anastasio C. 2014. Secondary organic aerosol production from aqueous reactions of atmospheric phenols with an organic triplet excited state. *Environ Sci Technol*. 48:1049–1057.
60 Zhang J, *et al*. 2024. Modeling novel aqueous particle and cloud chemistry processes of biomass burning phenols and their potential to form secondary organic aerosols. *Environ Sci Technol*. 58:3776–3786.
61 Jiang H, *et al*. 2023. Aqueous-Phase secondary processes and meteorological change promote the brown carbon formation and transformation during haze events. *J Geophys Res Atmos*. 128: e2023JD038735.
62 Chameides WL. 1986. Possible role of NO_3 in the nighttime chemistry of a cloud. *J Geophys Res Atmos*. 91:5331–5337.
63 Platt U, Heintz F. 2013. Nitrate radicals in tropospheric chemistry. *Isr J Chem*. 34:289–300.
64 Decker ZCJ, *et al*. 2019. Nighttime chemical transformation in biomass burning plumes: a box model analysis initialized with aircraft observations. *Environ Sci Technol*. 53:2529–2538.
65 Becke AD. 1993. Density-functional thermochemistry. III. The role of exact exchange. *J Chem Phys*. 98:5648–5652.
66 Grimme S, Ehrlich S, Goerigk L. 2011. Effect of the damping function in dispersion corrected density functional theory. *J Comput Chem*. 32:1456–1465.
67 Kendall RA, Dunning TH Jr, Harrison RJ. 1992. Electron affinities of the first-row atoms revisited. Systematic basis sets and wave functions. *J Chem Phys*. 96:6796–6806.
68 Marenich AV, Cramer CJ, Truhlar DG. 2009. Universal solvation model based on solute electron density and on a continuum model of the solvent defined by the bulk dielectric constant and atomic surface tensions. *J Phys Chem B*. 113:6378–6396.
69 Frisch M, *et al*. 2016. *Gaussian 16, Revision A*. 03. Wallingford, CT: Gaussian Inc.
70 Noga J, Bartlett RJ. 1987. The full CCSDT model for molecular electronic structure. *J Chem Phys*. 86:7041–7050.
71 Riplinger C, Neese F. 2013. An efficient and near linear scaling pair natural orbital based local coupled cluster method. *J Chem Phys*. 138:034106.

72 Riplinger C, Sandhoefer B, Hansen A, Neese F. 2013. Natural triple excitations in local coupled cluster calculations with pair natural orbitals. *J Chem Phys*. 139:134101.
73 Riplinger C, Pinski P, Becker U, Valeev EF, Neese F. 2016. Sparse maps—a systematic infrastructure for reduced-scaling electronic structure methods. II. Linear scaling domain based pair natural orbital coupled cluster theory. *J Chem Phys*. 144:024109.
74 Saitow M, Becker U, Riplinger C, Valeev EF, Neese F. 2017. A new near-linear scaling, efficient and accurate, open-shell domain-based local pair natural orbital coupled cluster singles and doubles theory. *J Chem Phys*. 146:164105.
75 Guo Y, *et al.* 2018. Communication: an improved linear scaling perturbative triples correction for the domain based local pair-natural orbital based singles and doubles coupled cluster method [DLPNO-CCSD(T)]. *J Chem Phys*. 148:011101.
76 Neese F. 2012. The ORCA program system. *WIREs Comput Mol Sci*. 2:73–78.
77 Lu T, Chen F. 2012. Multiwfn: a multifunctional wavefunction analyzer. *J Comput Chem*. 33:580–592.
78 Lu T, Chen Q. 2021. Shermo: a general code for calculating molecular thermochemistry properties. *Comput Theor Chem*. 1200: 113249.